

Sparse Reconstruction of Optical Doppler Tomography Based on State Space Model

Zhenghong Li, Jiaxiang Ren, Wensheng Cheng, Congwu Du, Yingtian Pan,
and Haibin Ling

Stony Brook University
{zhenghli,hling}@cs.stonybrook.edu

Abstract. Optical Doppler Tomography (ODT) is a blood flow imaging technique popularly used in bioengineering applications. The fundamental unit of ODT is the 1D frequency response along the A-line (depth), named raw A-scan. A 2D ODT image (B-scan) is obtained by first sensing raw A-scans along the B-line (width), and then constructing the B-scan from these raw A-scans via magnitude-phase analysis and post-processing. To obtain a high-resolution B-scan with a precise flow map, densely sampled A-scans are required in current methods, causing both computational and storage burdens. To address this issue, in this paper we propose a novel sparse reconstruction framework with four main sequential steps: 1) early magnitude-phase fusion that encourages rich interaction of the complementary information in magnitude and phase, 2) State Space Model (SSM)-based representation learning, inspired by recent successes in Mamba and VMamba, to naturally capture both the intra-A-scan sequential information and between-A-scan interactions, 3) an Inception-based Feedforward Network module (IncFFN) to further boost the SSM-module, and 4) a B-line Pixel Shuffle (BPS) layer to effectively reconstruct the final results. In the experiments on real-world animal data, our method shows clear effectiveness in reconstruction accuracy. As the first application of SSM for image reconstruction tasks, we expect our work to inspire related explorations in not only efficient ODT imaging techniques but also generic image enhancement.

Keywords: Optical Doppler Tomography · Sparse Reconstruction · State Space Model

1 Introduction

Optical Doppler Tomography (ODT), also named Doppler Optical Coherence Tomography (D-OCT), is an emerging technique for blood flow visualization and quantification [17]. ODT combines the Doppler principle with OCT to quantify blood flow velocity based on the Doppler effect of red blood cells [6]. It has advantages in acquiring high-resolution and high-contrast tomographic images [18], and has many potential clinical applications such as vascular disease diagnosis and monitoring [17].

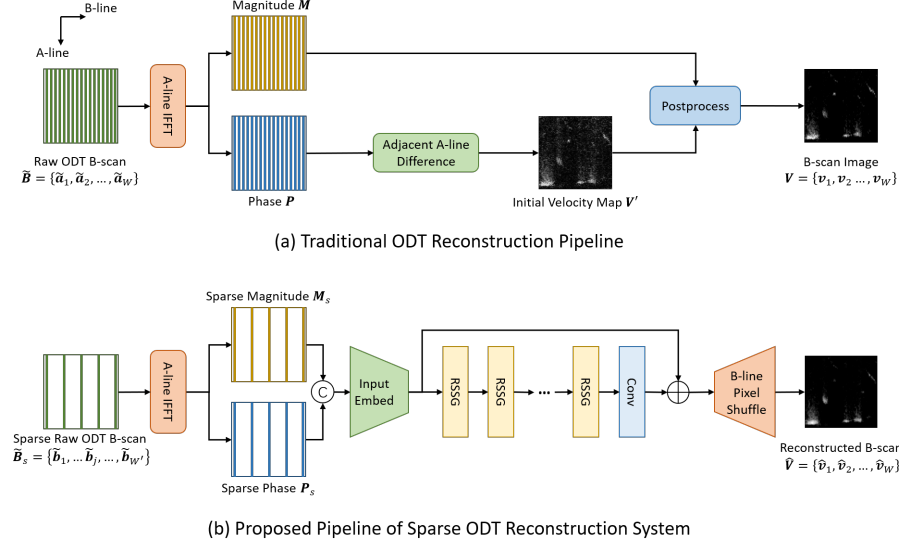


Fig. 1: ODT reconstruction. (a) A traditional ODT reconstruction pipeline as described in the text (Sec. 1). (b) Proposed pipeline of the sparse ODT reconstruction system. The sparse raw B-scan $\tilde{\mathbf{B}}_s$ is downsampled from $\tilde{\mathbf{B}}$ with a stride δ along the B-line, such that $\tilde{\mathbf{b}}_j = \tilde{\mathbf{a}}_{1+(j-1)\delta}$. $\tilde{\mathbf{B}}_s$ is forwarded to our neural network-based system to reconstruct $\hat{\mathbf{V}}$ with the same resolution as \mathbf{V} .

Figure 1 (a) illustrates a typical ODT image reconstruction pipeline. The basic scan of raw ODT signals is along the A-line called raw A-scan $\tilde{\mathbf{a}}_i \in \mathbb{R}^H$, which is the H -dimensional frequency domain response along depth. By sliding the scanning sensor along the B-line, we can get a 2D raw signal called raw B-scan $\tilde{\mathbf{B}} = \{\tilde{\mathbf{a}}_i\}_{i=1}^W$ containing W raw A-scans. To construct the final B-scan, the 1D Inverse Fast Fourier Transform (IFFT) is first applied to each raw A-scan to get the spatial domain magnitude $\mathbf{M} = \{\mathbf{m}_i\}_{i=1}^W$ and phase $\mathbf{P} = \{\mathbf{p}_i\}_{i=1}^W$. Then, the phase difference $\mathbf{v}'_i \in \mathbb{R}^H$ between adjacent A-lines is calculated to extract the Doppler frequency shift and get the velocity map of blood flow $\mathbf{V}' = \{\mathbf{v}'_i\}_{i=1}^W$ [22]. Finally, the velocity map \mathbf{V}' is post-processed and denoised, often with the help from the magnitude map \mathbf{M} , to obtain the final result $\mathbf{V} = \{\mathbf{v}_i \in \mathbb{R}^H\}_{i=1}^W$.

Although ODT is promising for blood flow velocity measurement, dense scanning of raw A-scans is required to get a precise estimation of the blood flow velocity, leading to serious memory and computation burden. A natural idea is to conduct the ODT reconstruction using sparsely sampled raw A-scans. As shown in Figure 1 (b), the goal is to reconstruct a high quality ODT image $\hat{\mathbf{V}} = \{\hat{\mathbf{v}}_i\}_{i=1}^W$ from sparsely sampled raw A-scans stored in $\tilde{\mathbf{B}}_s = \{\tilde{\mathbf{b}}_j = \tilde{\mathbf{a}}_{1+(j-1)\delta}\}_{j=1}^{W'}$, where δ is sampling stride along B-line, $W' = 1 + \text{floor}((W - 1)/\delta)$ is the number of sparsely sampled raw A-scans.

Straightforward implementation based on existing methods, however, sacrifices the reconstruction precision, partly due to the ignorance of the structural properties in the ODT imaging process as described above. In particular, there are two crucial distinctions between our task and related ones such as single image super-resolution (SISR). Primarily, in the sparse ODT reconstruction, the information is downsampled solely along the B-line, resulting in the information on the skipped A-lines being lost, while the information on the sampled A-line is well-kept. Conversely, classical SISR tasks involve isotropic downsampling and mixing of information from neighboring pixels. Secondly, in ODT B-scans, not only the magnitude and phase themselves but also the phase difference between adjacent A-scans has important physical significance. In contrast, although the gradients in generic images are also meaningful, it is not as significant as the phase difference in ODT reconstruction, and most of the classical SISR methods focus on the pixels themselves, not on the differences between them.

Specifically, regarding the anisotropic information downsampling challenge in sparse ODT signal processing, state-of-the-art classical SISR models [5, 19, 20, 41] based on vision transformers, may not be ideal for addressing this characteristic. The isotropic treatment of A-line and B-line information by the attention mechanism in vision transformers is a limiting factor. Furthermore, since a B-scan is fundamentally formed A-line-by-A-line, we propose to extract the features of the A-line and B-line separately to address this anisotropic characteristic better. For this purpose, utilizing a sequence model to individually scan the sequences of a B-scan feature map unfolded along the A-line and B-line is a promising solution. Recently, a State Space Model (SSM) named Mamba [9] has been proposed. With the strong long-range dependencies modeling ability and the linear computational complexity of the proposed selective SSM, Mamba is considered suitable for modeling the sequences from unfolded B-scan feature maps. In addition, Visual Mamba (VMamba) [23], an application of Mamba for visual tasks, has been recently introduced. VMamba proposes a 2D-Selective-Scan mechanism (SS2D) that unfolds a feature map into four sequences along rows and columns, and along the forward and backward directions, and employs the selective SSM to process these sequences individually. Inspired by these works, we propose to employ the Mamba and SS2D module for modeling the anisotropic information downsampling property in sparse ODT reconstruction.

To comprehensively model the characteristics in the reconstruction of sparse ODT raw images, in this paper, we proposed a Mamba-based Sparse optical Doppler tomography Reconstruction (MSDR) model. First, to encourage rich interaction of the magnitude and phase, we fuse them for the input embedding. Second, to address the anisotropic downsampling property, we propose utilizing an SSM that separately scans sequences of a B-scan feature map unfolded along the A-line and B-line. This approach is naturally appropriate to model this feature compared with attention-based methods. Third, to comprehensively model the magnitude, phase, and phase difference along the B-line, we propose a novel Inception-based [32, 33] feedforward network (FFN) that explicitly fuses the information from the deep features and their B-line differences. Finally, to

effectively upscale the B-line, drawing inspiration from the classical sub-pixel convolution [30], we employ a B-line pixel shuffle layer for reconstruction. To the best of our knowledge, this is the first work on sparse ODT reconstruction and the first instance of applying SSM-based models to tasks related to image reconstruction. Experiments demonstrate that our method has exhibited promising results in comparison with state-of-the-arts.

To summarize, our main contributions include: **(1)** the first sparse reconstruction pipeline, to our best knowledge, for ODT image generation, **(2)** the first application of SSM techniques for image reconstruction tasks, and **(3)** a novel Inception-based FFN module that effectively fuses the information from features and their B-line differences.

2 Related Works

2.1 Vision Transformer

Inspired by the success of transformers in natural language processing [34], vision transformers have been proposed for various vision tasks. Because of their better potential modeling abilities than CNNs [12, 16, 29, 31], vision transformers have been widely applied in various computer vision tasks in recent years such as image classification [8, 24], object detection [3, 38, 42], and segmentation [2, 35]. ViT [8] is one of the pioneer works of vision transformers that partition images into patches and take them as input tokens to the transformer for image classification. Because of the high computational consumption of the classical global attention mechanism, Liu *et al.* [24] proposes the Swin transformer to enable vision transformers applicable to high-resolution image inputs. Swin transformer employs window attention to lower the computational cost and uses the sliding window mechanism to exchange information across different windows. Zhang *et al.* [39] proposes a multi-scale vision transformer and an attention mechanism adopted from a natural language processing work [1]. Yang *et al.* [36] proposes an attention mechanism that incorporates both fine-grained local and coarse-grained global interactions, which can be plugged into multi-scale vision transformers and achieves good performance.

2.2 Image Super-Resolution

Early Single Image Super-Resolution (SISR) methods are mainly based on CNNs [7, 21, 27, 40]. Recently, vision transformer-based models have demonstrated promising performance in SISR tasks, attributed to their ability to capture global information effectively. IPT [4] applies a large pretrained transformer for super-resolution task. SwinIR [20] adopts the Swin attention mechanism [24] to capture the global information with acceptable computational complexity for SISR. GRL [19] proposed a mechanism to model the image hierarchies in global, regional, and local ranges via channel-wise attention, anchored stripe attention, and window attention respectively. The proposed anchored stripe attention is

supposed to be able to model the anisotropic information, but it does not explicitly model the information along different axes inside the stripes. Thus, this may limit its capability to handle the anisotropic downsampling in sparse ODT compared to capturing anisotropic information in generic images. SRFormer [41] proposes a permuted self-attention mechanism that balances the channel and spatial information for self-attention. DAT [5] proposes to alternatively apply spatial window and channel-wise attention and employ an adaptive interaction module to fuse the global and local features.

2.3 State Space Models

Classic State Space Models (SSMs) [15] are first proposed in the field of control, which describe the transformation of state spaces. Recently, deep models [9, 10] based on SSMs have been introduced for sequence modeling in deep learning. The Linear State Space Layer [11] conceptually proves that deep SSMs can address long-range dependencies in principle. But its direct application in practice is challenging due to the heavy computation and memory costs required by the state representation. To reduce the computational burden and build practical usable deep SSMs, S4 [10] proposes to condition the state matrix with a low-rank correction to reduce the computation and memory cost. Mamba [9] takes the SSM parameters as functions of the input to effectively select data in an input-dependent manner. A hardware-aware parallel algorithm in recurrent mode is also designed to improve the computational efficiency. These models can capture long-range dependencies in sequences through efficient computations that scale linearly or near-linearly with sequence length. VMamba [23] extends Mamba [9] to 2D images with the proposed 2D selective scan, and achieves promising results on visual recognition tasks.

3 Method

3.1 Problem Formulation

This study focuses on reconstructing the visualization $\hat{\mathbf{V}}$ from the sparse raw B-scans $\tilde{\mathbf{B}}_s$ to get the same resolution as the normally scanned visualization \mathbf{V} . There are two main properties of this task. First is the anisotropic information downsampling. Compared with normally scanned raw B-scans $\tilde{\mathbf{B}}$, the information downsampling is only along the B-line. This property suggests that a model that separately processes the information along the A-line and B-line may be appropriate for sparse ODT reconstruction. Second, in ODT reconstruction, the magnitude, phase, and phase differences along the B-line are all important for visualization. This property inspires us that a multi-branch block with feature difference inputs may comprehensively model the information in ODT B-scans. In the following subsections, we will demonstrate how we address these properties with our proposed MSDR model. We will first introduce the preliminaries of Mamba, then describe the overall pipeline, and finally demonstrate the details of the network blocks.

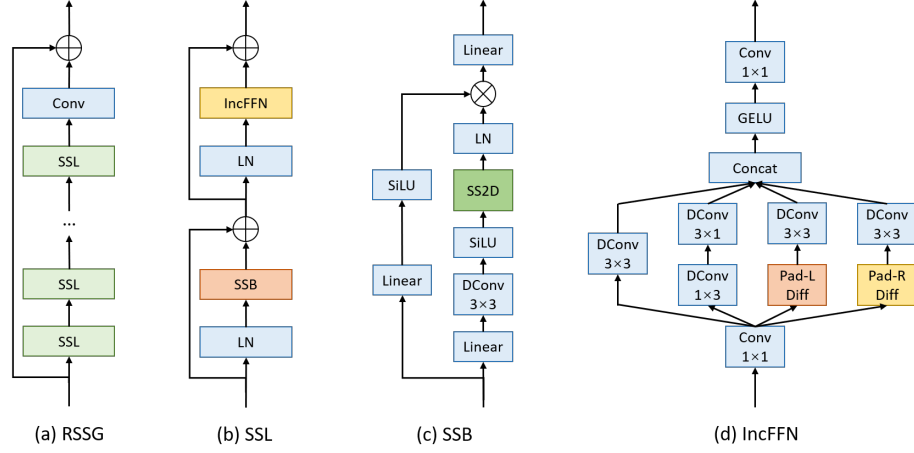


Fig. 2: Illustration of the network blocks. (a) Residual State Space Group (RSSG), (b) State Space Layer (SSL), (c) State Space Block (SSB), and (d) Inception-based Feedforward Network (IncFFN).

3.2 Preliminaries of Mamba

Mamba [9] is a recently introduced 1D structured state space sequence model. Structured State Space Sequence Models (S4) [10] is a recently proposed class of deep sequence models. These models describe a continuous sequence-to-sequence translation system that maps a 1D sequence $x(t) \in \mathbb{R}$ to $y(t) \in \mathbb{R}$ via latent states $h(t) \in \mathbb{R}^N$, where N is the state size. It can be formulated as linear ordinary differential equations:

$$h'(t) = \mathbf{A}h(t) + \mathbf{B}x(t), \quad y(t) = \mathbf{C}h(t), \quad (1)$$

where the state matrix $\mathbf{A} \in \mathbb{R}^{N \times N}$ and vectors $\mathbf{B}, \mathbf{C} \in \mathbb{R}^{N \times 1}$ are parameters.

To get the model of a continuous system working for deep learning, discretization will be applied to the parameters. The zero-order hold rule is usually utilized to discretize them as:

$$\bar{\mathbf{A}} = \exp(\Delta\mathbf{A}), \quad \bar{\mathbf{B}} = (\Delta\mathbf{A})^{-1}(\exp(\Delta\mathbf{A}) - \mathbf{I} \cdot \Delta\mathbf{B}), \quad (2)$$

where $\Delta \in \mathbb{R}_{>0}$ is a parameter of sample time. In this way, the system can be represented as:

$$\begin{aligned} h_t &= \bar{\mathbf{A}}h_{t-1} + \bar{\mathbf{B}}x_t, \\ y_t &= \mathbf{C}h_t. \end{aligned} \quad (3)$$

In classical S4 models, the above system is linear time-invariant (LTI), where the parameters $\bar{\mathbf{A}}, \bar{\mathbf{B}}$ are fixed for all time-step. Although the LTI constraint is efficient, it sometimes limits the ability of the system to model certain types

of sequences. To address this issue, Mamba removes the LTI constraint, and instead, introduces a selective scan mechanism (selective SSM), which makes the parameters $\bar{\mathbf{B}}, \mathbf{C} \in \mathbb{R}^{B \times L \times N}$ and $\Delta \in \mathbb{R}^{B \times L \times D}$ functions of the input sequence $\mathbf{x} \in \mathbb{R}^{B \times L \times D}$, where B is the batch size, L is the sequence length, and D is the input dimension.

Given the anisotropic downsampling property observed in the sparse ODT reconstruction task, we aim to handle information along the A-line and B-line distinctly. Therefore, utilizing a sequence model to separately process a B-scan feature map unfolded along the A-line and B-line is a promising solution. Considering the strong sequence modeling capabilities of Mamba with the linear computational complexity, we propose employing Mamba to individually scan the ODT B-scan feature map along the A-line and B-line to model this property.

3.3 Overall Pipeline

The overall pipeline is presented in Fig. 1(b). The input to the whole system is a sparsely sampled raw ODT B-scan $\tilde{\mathbf{B}}_s$. We first employ an input embedding module to encode it to deep feature representations. Following the traditional process, 1D IFFT is applied to each raw A-scan $\tilde{\mathbf{b}}_j$ in $\tilde{\mathbf{B}}_s$. We then concatenate the transformed sparse spatial magnitude and phase as the input (denoted as \mathbf{X}_{in}) to the network. The framework of the network mainly refers to [20]. The network input is first encoded via a convolution layer and then processed by a sequence of Residual State Space Groups (RSSG), where state space model-based blocks and Inception-based feedforward network blocks will be utilized to model deep features. Before the residual link, the extracted features will be processed by another convolution layer. Finally, drawing from classical SISR methods [30], a B-line Pixel Shuffle (BPS) layer is employed to upsample the B-line by first expanding the channel dimension and then rearranging the feature map to expand the B-line. In summary, the network can be represented as:

$$\begin{aligned} \mathbf{X}_0 &= \text{Conv}(\mathbf{X}_{in}), \\ \mathbf{X}_g &= \text{RSSG}_g(\mathbf{X}_{g-1}), \\ \hat{\mathbf{V}} &= \text{BPS}(\mathbf{X}_0 + \text{Conv}(\mathbf{X}_R)), \end{aligned} \quad (4)$$

where $g = 1, 2, \dots, G$ is the index of the RSSG. We employ the pixel L_2 loss as the optimization function.

3.4 Input Embedding

The input to the sparse ODT reconstruction system is a sparse raw B-scan $\tilde{\mathbf{B}}_s$. Following the traditional pipeline, 1D IFFT will be applied to each raw A-scan $\tilde{\mathbf{b}}_j$ to transform the information from the frequency domain representation to the spatial magnitude \mathbf{M}_s and phase \mathbf{P}_s responses, where the A-line indices follow $\tilde{\mathbf{B}}_s$. To encourage rich interaction of the complementary information in magnitude and phase, we concatenate them along the channel dimension together as



Fig. 3: Illustration of the SS2D block [23] on a B-scan feature map. Each column with the same color in the input represents an A-line, and each row in the input represents a B-line. The input feature map will be unfolded along the A-line and B-line, as well as along the forward and backward directions. The four unfolded sequences will be scanned via the selective SSM proposed in Mamba [9]. Finally, the processed sequences will be folded back and merged via summation.

the input to the network. We then encode the input map to a deep embedding via a convolution layer for the following deep feature extractions.

3.5 Residual State Space Group

A Residual State Space Group (RSSG) consists of a sequence of State Space Layers (SSL) and a convolution layer. The architecture is inspired by [20] and is presented in Fig. 2(a). The input feature will be forwarded sequentially to these layers and then added with the input itself. The overall architecture of the g -th RSSG can be represented as:

$$\begin{aligned} \mathbf{X}_{g,r} &= \text{SSL}_{g,r}(\mathbf{X}_{g,r-1}), \\ \mathbf{X}_{g,\text{out}} &= \mathbf{X}_{g,0} + \text{Conv}(\mathbf{X}_{g,r}), \end{aligned} \quad (5)$$

where $r = 1, 2, \dots, R$ is the index of a SSL in a RSSG, $\mathbf{X}_{g,0}$ equals the \mathbf{X}_{g-1} in Eq. 4, which is the output of the last RSSG, and $\mathbf{X}_{g,\text{out}}$ equals the \mathbf{X}_g in Eq. 4, which is the output of the g -th RSSG.

The architecture of a SSL is presented in Fig. 2(b). In general, the pipeline refers to transformer-based models [20, 34], which can be represented as:

$$\begin{aligned} \mathbf{X}'_{g,r} &= \mathbf{X}_{g,r-1} + \text{SSB}_{g,r}(\text{LN}(\mathbf{X}_{g,r-1})), \\ \mathbf{X}_{g,r} &= \mathbf{X}'_{g,r} + \text{IncFFN}_{g,r}(\text{LN}(\mathbf{X}'_{g,r})), \end{aligned} \quad (6)$$

where LN denotes the LayerNorm operation.

In the following paragraphs, we will specifically demonstrate the two key blocks of the SSL: State Space Block (SSB) and Inception-based Feedforward Network (IncFFN), and how they are effective for modeling the sparse ODT reconstruction properties.

State Space Block The State Space Block (SSB) is inspired by [9, 23]. In sparse ODT B-scans, the information downsampling is only along the B-line.

Thus, compared with the widely applied 2D attention-based models isotropically processing an image, a sequence module separately scanning information along the A-line and B-line is considered more appropriate for this anisotropic property. Recently, Mamba [9], a new SSM, has shown strong sequence modeling capability with linear complexity. Hence, we propose employing Mamba to scan the A-line and B-line of an ODT B-scan feature map. The recent Mamba application for visual tasks, VMamba [23], unfolds image feature maps into four sequences along rows and columns, as well as forward and backward directions, and applies the selective SSM of Mamba for scanning (named SS2D). Inspired by this work, we adopt such processing to model the B-scan. The structure of an SSB is illustrated in Fig. 2(c). Given an input \mathbf{X} , an SSB can be represented as:

$$\begin{aligned}\mathbf{X}_1 &= \text{SiLU}(\text{Linear}(\mathbf{X})), \\ \mathbf{X}_2 &= \text{LN}\left(\text{SS2D}(\text{SiLU}(\text{DConv}(\text{Linear}(\mathbf{X}))))\right), \\ \mathbf{X}_{\text{out}} &= \text{Linear}(\mathbf{X}_1 \odot \mathbf{X}_2),\end{aligned}\tag{7}$$

where SiLU [13, 28] is the activation function, DConv denotes the depth-wise convolution, SS2D is the aforementioned block whose procedure is demonstrated in Fig. 3, and \odot denotes the element-wise product.

Inception-based Feedforward Network In ODT reconstruction pipelines, not only the magnitude and phase but also the phase difference along the B-line has important physical significance. However, classical Multi-layer perceptron-based (MLP) Feedforward networks (FFN) do not explicitly model the feature difference. To comprehensively model the properties of the features, a multi-branch network block is an effective solution. Drawing inspiration from the Inception block [32], we propose an Inception-based FFN (IncFFN) as depicted in Fig. 2(d) to address this issue. Specifically, after the input embedding layer, we explicitly incorporate a 1D difference operation along the B-line to the features. Besides, to maintain the size of the feature map, zero padding to the left or right will be applied. We denote these operations as Pad-L Diff (or PLD) and Pad-R Diff (or PRD). With the multi-branch design, both the feature and the feature difference along the B-line will be explicitly processed, guiding the network to perform comprehensive modeling. Given an input \mathbf{X} , the Inception-based FFN can be represented as:

$$\begin{aligned}\mathbf{X}_0 &= \text{Conv}(\mathbf{X}), \\ \mathbf{X}_1 &= \text{DConv}(\mathbf{X}_0), \\ \mathbf{X}_2 &= \text{DConv}(\text{DConv}(\mathbf{X}_0)), \\ \mathbf{X}_3 &= \text{DConv}(\text{PLD}(\mathbf{X}_0)), \\ \mathbf{X}_4 &= \text{DConv}(\text{PRD}(\mathbf{X}_0)), \\ \mathbf{X}_{\text{out}} &= \text{Conv}(\text{GELU}(\text{Concat}([\mathbf{X}_1, \mathbf{X}_2, \mathbf{X}_3, \mathbf{X}_4]))),\end{aligned}\tag{8}$$

where Concat denotes the concatenation operation and GELU [13] is the activation function.

3.6 B-line Pixel Shuffle

Since in sparse ODT reconstruction, only the B-line needs to be upsampled, we propose a B-line Pixel Shuffle (BPS) layer, modified from the classical sub-pixel convolution layer [30]. For classical SISR, a sub-pixel convolution layer is widely applied to isotropically upsample the feature map. Specifically, it first employs a convolution layer to expand the channel dimension and then rearranges the feature map by shrinking the channel dimension back while increasing the height and width equally. Following a similar process, since only the B-line is downsampled in the sparse ODT reconstruction, a BPS layer only rearranges the channel and width (B-line) dimension to upsample the B-line.

4 Experiments

4.1 ODT Dataset of Mouse Brain Cortex

Collecting animals’ vasculature data is complex, leading most related works to utilize small datasets [14, 18]. In this work, we collected 17 ODT volumes of mouse brain cortex, with 12 volumes in the training set and 5 in the test set. Both sets encompass volumes from awake mice, anesthetized mice, and intralipid-enhanced imaging, ensuring comprehensive evaluation. Each volume includes 500 densely scanned raw B-scans. Each raw B-scan measures 2048×12600 , meaning it contains 12600 raw A-scans with a depth of 2048. Following traditional pipelines, we reconstruct each B-scan visualization to 512×12600 .

For a practical evaluation, we compare the inferred volumes with test targets after the post-processing of the B-scan shape. Following traditional pipelines, a reshape-crop-shear operation will be applied to make the processed volume appropriate for presentation. Since the dense scanning causes distorted aspect ratios, the reconstructed B-scans will be first reshaped to 512×1000 . Additionally, deep background noise will be cropped out, and a shear transformation will align the depth of B-scans in a volume. After the reshape-crop-shear operation, a volume is typically around $500 \times 250 \times 1000$ with high information density suitable for 3D presentation. The same operations will be applied to the pairs of a test target volume and its corresponding predicted volumes. Moreover, since Maximum Intensity Projection (MIP) along the depth is common for the 2D visualization of 3D vasculature volumes [14, 17, 18], we will also assess results on the MIP images of the processed volumes.

4.2 Implementation Details

We conduct experiments with the sparse downsampling factor as 4. In the proposed MSDR, the number of RSSG and SSL are generally set to 4 and 6. The embedding dimension of features is set to 56. The input size of a raw B-scan patch is 2048×64 . After the IFFT-related transforms, the spatial size of the input to the networks is 512×64 whose depth is the same as the target visualization. The batch size is set to 8. We employ AdamW [26] as the optimizer

with $\beta_1 = 0.9$, $\beta_2 = 0.95$, and weight decay = $1e - 4$. The number of training iterations is set to 20K. The learning rate scheduler is CosineAnnealingLR [25] whose initial and minimum learning rates are set to $3e - 4$ and $1e - 6$.

We compare our method with recently published state-of-the-art classical SISR methods: SwinIR [20], GRL [19], SRFormer [41], and DAT [5]. We apply the same input embedding method as ours, and we replace the sub-pixel convolution layer in their high-resolution reconstruction module with our BPS layer to make them applicable to this sparse ODT reconstruction task. We follow their default network parameters. The batch sizes are set to fulfill the GPU memory, and the other training configurations are the same for a fair comparison. All experiments are carried out on two NVIDIA A6000 GPUs.

For the evaluation metrics, as mentioned above, we evaluate the results in two aspects: B-scan and MIP. In the experiments, we calculate the PSNR and SSIM on each B-scan and each MIP image and present both of them in the quantitative evaluations.

4.3 Quantitative Results

The experimental results of various methods on sparse ODT reconstruction with a downsampling factor of 4 are summarized in Table 1. Our method MSDR clearly outperforms others on all metrics. It’s worth noting that SwinIR and SRFormer primarily rely on spatial window attention, while GRL and DAT incorporate both spatial window attention and channel-wise attention. Except for our method, the other methods are mainly based on single-branch FFNs. The result implies that channel-wise attention may improve performance. However, both channel-wise and spatial-wise attention naturally treat the A-line and B-line together, which may not be appropriate to model the anisotropic downsampling property in sparse ODT B-scans. Particularly, the anchored stripe attention, a variant of the spatial-wise attention proposed in GRL, is supposed to have the ability to model the anisotropic image features. However, the result shows that it is not effective for modeling the anisotropic downsampling property in this task. This might be because it does not explicitly model the information along different axes inside a stripe. Thus, although it may work for generic images, it does not perform well in sparse ODT reconstruction. Additionally, single-branch FFNs may not adequately capture the properties of magnitude, phase, and phase difference comprehensively, due to their limited modeling capability.

4.4 Qualitative Results

Because the visualization of the reconstructed B-scans is not intuitive, following the common 3D vasculature visualization process [14, 17, 18], we directly present the MIP images of the predicted volumes. Fig. 4 compares the MIP images of (a) SwinIR [20], (b) GRL [19], (c) SRFormer [41], (d) DAT [5], (e) MSDR, and (f) groundtruth (GT). The regions of interest are zoomed in and the challenging cases are further highlighted by colored arrows. There are typically two main challenges in sparse reconstructed ODT volumes: continuity of small vessels and

Table 1: Comparison of sparse ODT reconstruction results

Method	B-scan		MIP	
	PSNR	SSIM	PSNR	SSIM
SwinIR [20]	33.80	0.894	19.80	0.546
GRL [19]	33.98	0.900	20.25	0.572
SRFormer [41]	33.86	0.895	19.81	0.546
DAT [5]	34.11	0.900	20.07	0.563
MSDR (ours)	34.93	0.907	21.03	0.622

Table 2: Comparison of the visual state space block with attention blocks

Method	B-scan		MIP	
	PSNR	SSIM	PSNR	SSIM
Swin Attn	34.16	0.898	20.36	0.575
Channel Attn	34.41	0.900	20.46	0.590
SSB	34.93	0.907	21.03	0.622

Table 3: Comparison of different feed-forward networks

Method	B-scan		MIP	
	PSNR	SSIM	PSNR	SSIM
MLP	34.81	0.906	21.02	0.617
w/o FFN	34.78	0.906	21.06	0.616
IncFFN	34.93	0.907	21.03	0.622

contrast. (1) The primary challenge lies in the continuity of small vessels. Due to slow blood flow in small vessels, their signals are often weak in ODT B-scans. Consequently, some small vessel signals may be lost in sparse reconstruction, impacting the continuity of reconstructed small vessels. As illustrated by the green arrows in Fig. 4, only our MSDR method can clearly preserve continuity in the highlighted vessel, while in the results of other methods, that part of the vessel is almost broken. (2) Another significant challenge is contrast. Given that input raw B-scans are sparse, most networks tend to over-smooth reconstructed volumes to minimize L_2 loss. This often leads to low contrast in Maximum Intensity Projection (MIP) results. As indicated by the yellow arrows in Fig. 4, the contrast of results from other methods in that area is relatively low, whereas our MSDR method can achieve contrast approaching the groundtruth. In summary, leveraging the contributions of SSB and IncFFN, our MSDR method produces promising visualization results of sparse reconstructed ODT.

4.5 Ablation Study

State Space Block To verify the contribution of the SSB to the performance, we carry out experiments by replacing the SSB in our MSDR method with a Swin attention block [20, 24] (also referred to as a spatial window attention block) and a channel-wise attention block [5, 37]. By default, the number of heads is set to 8. For the Swin attention, the window size is set to 8. The experimental results

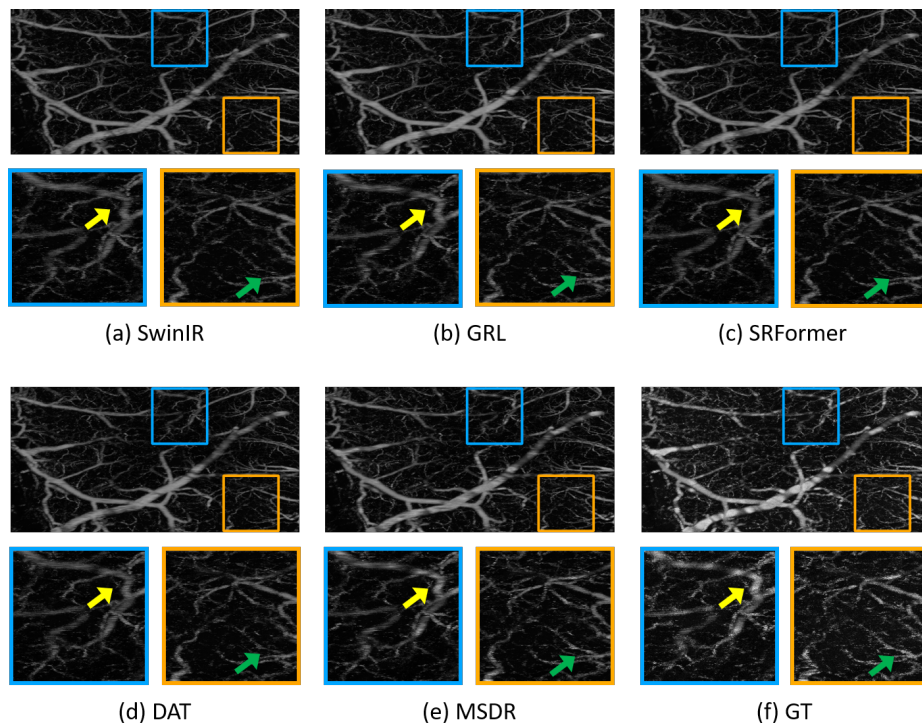


Fig. 4: Qualitative comparison of MIP results. Regions of interest are zoomed in. Colored arrows are further utilized to mark the challenging cases in the zoom-in regions.

are summarized in Table 2. It’s observed that compared to attention blocks, SSB achieved better performance in sparse ODT reconstruction. This is because SSB separately processes the ODT B-scan feature maps unfolded along the A-line and B-line, enabling better capture of the anisotropic information downsampling property in sparse ODT. In contrast, the attention mechanisms do not explicitly discern the information along the A-line and B-line but process them together, which may not be suitable for modeling this property. Additionally, the channel-wise attention block outperforms the Swin attention in this task. This could be attributed to the fact that channel-wise attention directly processes global information, whereas Swin attention relies on sliding spatial windows to capture global information and focuses on processing spatial information, which may be more prone to confusion by information along different axes.

Inception-based Feedforward Network To investigate the impact of our proposed IncFFN, we conduct experiments on substituting the IncFFN with the classical MLP-based FFN. Besides, in the paper of Mamba [9], the authors claim that MLP is not necessary for mamba-based models, we further carry out experiments by removing the FFN in the SSL. The experiment results are presented

in Table 3. Compared with the model without FFN, simply applying MLP as the FFN does not cause much difference. However, with the contribution of our IncFFN, the performance on the sparse ODT reconstruction is clearly improved. This is because the IncFFN employs a multi-branch design, which explicitly processes both the input feature and its difference along the B-line. This structure enables the network to comprehensively process the information in magnitude, phase, and phase difference. Thus, our IncFFN method can effectively improve the sparse ODT reconstruction.

5 Conclusion

This paper proposes an effective state space model-based method for sparse reconstruction of ODT. This task has two main properties, anisotropic information downsampling and processing multiple aspects of data. For modeling the anisotropic information downsampling, we propose to unfold the B-scan feature map into sequences along the A-line and B-line and employ Mamba, a state space model to separately process the sequences. For processing the multiple aspects of data, i.e., magnitude, phase, and the difference of phase along the B-line, we propose an Inception-based feedforward network to explicitly fuse the information from the features and their difference along the B-line. Experiments on an ODT dataset of mouse brain cortex show that our method effectively reconstructs precise high-resolution blood flow volumes from sparse ODT raw volumes. Furthermore, this work is expected to serve as foundational research for future efforts aimed at reconstructing accelerated ODT data obtained through sparse scanning along the B-line.

References

1. Beltagy, I., Peters, M.E., Cohan, A.: Longformer: The long-document transformer. arXiv preprint arXiv:2004.05150 (2020) [4](#)
2. Cao, H., Wang, Y., Chen, J., Jiang, D., Zhang, X., Tian, Q., Wang, M.: Swin-unet: Unet-like pure transformer for medical image segmentation. In: European conference on computer vision. pp. 205–218. Springer (2022) [4](#)
3. Carion, N., Massa, F., Synnaeve, G., Usunier, N., Kirillov, A., Zagoruyko, S.: End-to-end object detection with transformers. In: European conference on computer vision. pp. 213–229. Springer (2020) [4](#)
4. Chen, H., Wang, Y., Guo, T., Xu, C., Deng, Y., Liu, Z., Ma, S., Xu, C., Xu, C., Gao, W.: Pre-trained image processing transformer. In: Proceedings of the IEEE/CVF conference on computer vision and pattern recognition. pp. 12299–12310 (2021) [4](#)
5. Chen, Z., Zhang, Y., Gu, J., Kong, L., Yang, X., Yu, F.: Dual aggregation transformer for image super-resolution. In: Proceedings of the IEEE/CVF International Conference on Computer Vision. pp. 12312–12321 (2023) [3](#), [5](#), [11](#), [12](#), [18](#)
6. Chen, Z., Zhang, J.: Doppler optical coherence tomography. *Optical Coherence Tomography: Technology and Applications* pp. 621–651 (2008) [1](#)
7. Dai, T., Cai, J., Zhang, Y., Xia, S.T., Zhang, L.: Second-order attention network for single image super-resolution. In: Proceedings of the IEEE/CVF conference on computer vision and pattern recognition. pp. 11065–11074 (2019) [4](#)

8. Dosovitskiy, A., Beyer, L., Kolesnikov, A., Weissenborn, D., Zhai, X., Unterthiner, T., Dehghani, M., Minderer, M., Heigold, G., Gelly, S., et al.: An image is worth 16x16 words: Transformers for image recognition at scale. In: International Conference on Learning Representations (2020) [4](#)
9. Gu, A., Dao, T.: Mamba: Linear-time sequence modeling with selective state spaces. arXiv preprint arXiv:2312.00752 (2023) [3](#), [5](#), [6](#), [8](#), [9](#), [13](#)
10. Gu, A., Goel, K., Re, C.: Efficiently modeling long sequences with structured state spaces. In: International Conference on Learning Representations (2021) [5](#), [6](#)
11. Gu, A., Johnson, I., Goel, K., Saab, K., Dao, T., Rudra, A., Ré, C.: Combining recurrent, convolutional, and continuous-time models with linear state space layers. *Advances in neural information processing systems* **34**, 572–585 (2021) [5](#)
12. He, K., Zhang, X., Ren, S., Sun, J.: Deep residual learning for image recognition. In: Proceedings of the IEEE conference on computer vision and pattern recognition. pp. 770–778 (2016) [4](#)
13. Hendrycks, D., Gimpel, K.: Gaussian error linear units (gelus). arXiv preprint arXiv:1606.08415 (2016) [9](#)
14. Jiang, Z., Huang, Z., Qiu, B., Meng, X., You, Y., Liu, X., Liu, G., Zhou, C., Yang, K., Maier, A., et al.: Comparative study of deep learning models for optical coherence tomography angiography. *Biomedical optics express* **11**(3), 1580–1597 (2020) [10](#), [11](#)
15. Kalman, R.E.: A new approach to linear filtering and prediction problems (1960) [5](#)
16. Krizhevsky, A., Sutskever, I., Hinton, G.E.: Imagenet classification with deep convolutional neural networks. *Advances in neural information processing systems* **25** (2012) [4](#)
17. Leitgeb, R.A., Werkmeister, R.M., Blatter, C., Schmetterer, L.: Doppler optical coherence tomography. *Progress in retinal and eye research* **41**, 26–43 (2014) [1](#), [10](#), [11](#)
18. Li, A., Du, C., Volkow, N.D., Pan, Y.: A deep-learning-based approach for noise reduction in high-speed optical coherence doppler tomography. *Journal of biophotonics* **13**(10), e202000084 (2020) [1](#), [10](#), [11](#)
19. Li, Y., Fan, Y., Xiang, X., Demandolx, D., Ranjan, R., Timofte, R., Van Gool, L.: Efficient and explicit modelling of image hierarchies for image restoration. In: Proceedings of the IEEE/CVF Conference on Computer Vision and Pattern Recognition. pp. 18278–18289 (2023) [3](#), [4](#), [11](#), [12](#), [18](#)
20. Liang, J., Cao, J., Sun, G., Zhang, K., Van Gool, L., Timofte, R.: Swinir: Image restoration using swin transformer. In: Proceedings of the IEEE/CVF international conference on computer vision. pp. 1833–1844 (2021) [3](#), [4](#), [7](#), [8](#), [11](#), [12](#), [18](#)
21. Lim, B., Son, S., Kim, H., Nah, S., Mu Lee, K.: Enhanced deep residual networks for single image super-resolution. In: Proceedings of the IEEE conference on computer vision and pattern recognition workshops. pp. 136–144 (2017) [4](#)
22. Liu, G., Lin, A.J., Tromberg, B.J., Chen, Z.: A comparison of doppler optical coherence tomography methods. *Biomedical optics express* **3**(10), 2669–2680 (2012) [2](#)
23. Liu, Y., Tian, Y., Zhao, Y., Yu, H., Xie, L., Wang, Y., Ye, Q., Liu, Y.: Vmamba: Visual state space model. arXiv preprint arXiv:2401.10166 (2024) [3](#), [5](#), [8](#), [9](#)
24. Liu, Z., Lin, Y., Cao, Y., Hu, H., Wei, Y., Zhang, Z., Lin, S., Guo, B.: Swin transformer: Hierarchical vision transformer using shifted windows. In: Proceedings of the IEEE/CVF international conference on computer vision. pp. 10012–10022 (2021) [4](#), [12](#)

25. Loshchilov, I., Hutter, F.: Sgdr: Stochastic gradient descent with warm restarts. In: International Conference on Learning Representations (2016) [11](#)
26. Loshchilov, I., Hutter, F.: Decoupled weight decay regularization. In: International Conference on Learning Representations (2018) [10](#)
27. Niu, B., Wen, W., Ren, W., Zhang, X., Yang, L., Wang, S., Zhang, K., Cao, X., Shen, H.: Single image super-resolution via a holistic attention network. In: Computer Vision–ECCV 2020: 16th European Conference, Glasgow, UK, August 23–28, 2020, Proceedings, Part XII 16. pp. 191–207. Springer (2020) [4](#)
28. Ramachandran, P., Zoph, B., Le, Q.V.: Searching for activation functions. arXiv preprint arXiv:1710.05941 (2017) [9](#)
29. Ronneberger, O., Fischer, P., Brox, T.: U-net: Convolutional networks for biomedical image segmentation. In: Medical Image Computing and Computer-Assisted Intervention–MICCAI 2015: 18th International Conference, Munich, Germany, October 5–9, 2015, Proceedings, Part III 18. pp. 234–241. Springer (2015) [4](#)
30. Shi, W., Caballero, J., Huszár, F., Totz, J., Aitken, A.P., Bishop, R., Rueckert, D., Wang, Z.: Real-time single image and video super-resolution using an efficient sub-pixel convolutional neural network. In: Proceedings of the IEEE conference on computer vision and pattern recognition. pp. 1874–1883 (2016) [4](#), [7](#), [10](#)
31. Simonyan, K., Zisserman, A.: Very deep convolutional networks for large-scale image recognition. In: 3rd International Conference on Learning Representations (ICLR 2015). Computational and Biological Learning Society (2015) [4](#)
32. Szegedy, C., Liu, W., Jia, Y., Sermanet, P., Reed, S., Anguelov, D., Erhan, D., Vanhoucke, V., Rabinovich, A.: Going deeper with convolutions. In: Proceedings of the IEEE conference on computer vision and pattern recognition. pp. 1–9 (2015) [3](#), [9](#)
33. Szegedy, C., Vanhoucke, V., Ioffe, S., Shlens, J., Wojna, Z.: Rethinking the inception architecture for computer vision. In: Proceedings of the IEEE conference on computer vision and pattern recognition. pp. 2818–2826 (2016) [3](#)
34. Vaswani, A., Shazeer, N., Parmar, N., Uszkoreit, J., Jones, L., Gomez, A.N., Kaiser, Ł., Polosukhin, I.: Attention is all you need. *Advances in neural information processing systems* **30** (2017) [4](#), [8](#)
35. Xie, E., Wang, W., Yu, Z., Anandkumar, A., Alvarez, J.M., Luo, P.: Segformer: Simple and efficient design for semantic segmentation with transformers. *Advances in Neural Information Processing Systems* **34**, 12077–12090 (2021) [4](#)
36. Yang, J., Li, C., Zhang, P., Dai, X., Xiao, B., Yuan, L., Gao, J.: Focal self-attention for local-global interactions in vision transformers. arXiv preprint arXiv:2107.00641 (2021) [4](#)
37. Zamir, S.W., Arora, A., Khan, S., Hayat, M., Khan, F.S., Yang, M.H.: Restormer: Efficient transformer for high-resolution image restoration. In: Proceedings of the IEEE/CVF conference on computer vision and pattern recognition. pp. 5728–5739 (2022) [12](#)
38. Zhang, H., Li, F., Liu, S., Zhang, L., Su, H., Zhu, J., Ni, L.M., Shum, H.Y.: Dino: Detr with improved denoising anchor boxes for end-to-end object detection. arXiv preprint arXiv:2203.03605 (2022) [4](#)
39. Zhang, P., Dai, X., Yang, J., Xiao, B., Yuan, L., Zhang, L., Gao, J.: Multi-scale vision longformer: A new vision transformer for high-resolution image encoding. In: Proceedings of the IEEE/CVF international conference on computer vision. pp. 2998–3008 (2021) [4](#)
40. Zhang, Y., Li, K., Li, K., Wang, L., Zhong, B., Fu, Y.: Image super-resolution using very deep residual channel attention networks. In: Proceedings of the European conference on computer vision (ECCV). pp. 286–301 (2018) [4](#)

41. Zhou, Y., Li, Z., Guo, C.L., Bai, S., Cheng, M.M., Hou, Q.: Srformer: Permuted self-attention for single image super-resolution. arXiv preprint arXiv:2303.09735 (2023) [3](#), [5](#), [11](#), [12](#), [18](#)
42. Zhu, X., Su, W., Lu, L., Li, B., Wang, X., Dai, J.: Deformable detr: Deformable transformers for end-to-end object detection. arXiv preprint arXiv:2010.04159 (2020) [4](#)

A Quantitative Result on B-line Downsampling Factor 2

Table 4 summarizes the experimental results of SwinIR [20], GRL [19], SRFormer [41], DAT [5], and our MSDR on sparse ODT reconstruction with a downsampling factor of 2 along the B-line. Similar to the results in Table 1 in the main paper, in this experiment, our proposed MSDR also outperforms the other methods. This superiority stems from the utilization of the state space model to process information along the A-line and B-line separately, along with the proposed novel Inception-based Feedforward Network (IncFFN) that fuses information from multiple aspects of the feature maps, enabling comprehensive modeling of magnitude, phase, and phase difference.

Table 4: Comparison of sparse ODT reconstruction results on downsampling factor 2

Method	B-scan		MIP	
	PSNR	SSIM	PSNR	SSIM
SwinIR [20]	36.47	0.925	22.35	0.733
GRL [19]	37.14	0.929	23.23	0.765
SRFormer [41]	36.85	0.927	22.93	0.751
DAT [5]	37.14	0.929	23.25	0.766
MSDR (ours)	38.00	0.934	24.67	0.809

B Qualitative Result on B-line Downsampling Factor 2

Fig. 5 compares the Maximum Intensity Projection (MIP) images of (a) SwinIR [20], (b) GRL [19], (c) SRFormer [41], (d) DAT [5], (e) MSDR, and (f) groundtruth (GT) for sparse ODT reconstruction with the B-line downsampling factor of 2. The regions of interest are zoomed in and colored arrows are employed to mark the challenging cases. Regarding the primary challenge in small vessel continuity, our MSDR outperforms the other methods. For the small vessel highlighted by the green arrows, the result of MSDR is still continuous, while the other results are almost broken. Regarding the challenge of image contrast, although it is somewhat alleviated compared to the experiment with a downsampling factor of 4, MSDR still shows better performance in solving this problem compared to other methods. Illustrated by the vessel marked by yellow arrows, the contrast of MSDR is closer to the groundtruth, resulting in a more precise imaging outcome.

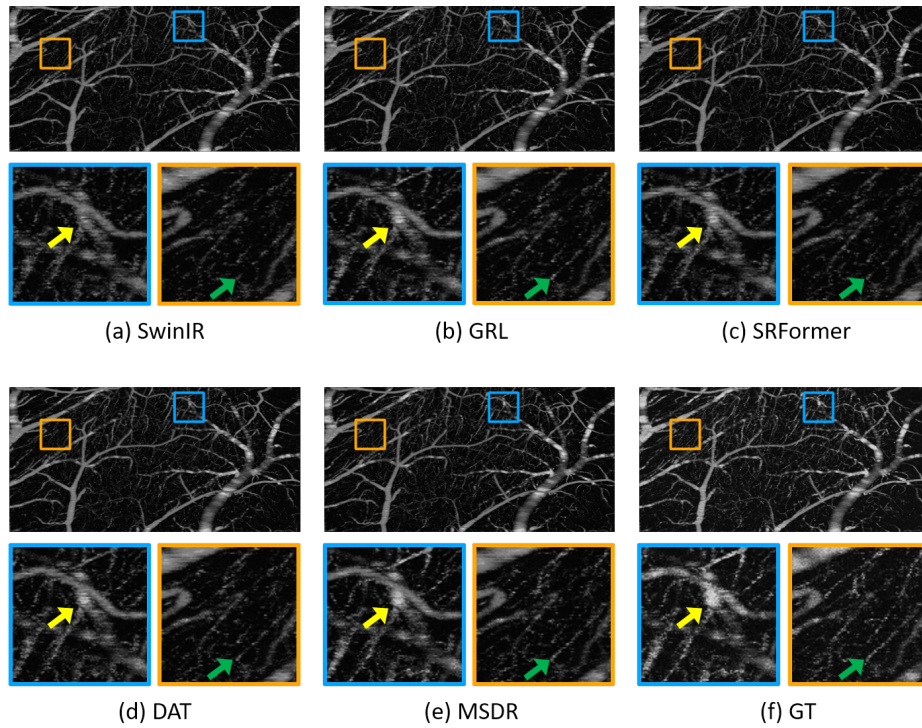


Fig. 5: Qualitative comparison of MIP results. Regions of interest are zoomed in. Colored arrows are further utilized to mark the challenging cases in the zoom-in regions.